Published in final edited form as:
IEEE J Sel Top Appl Earth Obs Remote Sens. 2019 May ; 12(5): 1599–1611. doi:10.1109/JSTARS.2019.2910565.

Response of GNSS-R on Dynamic Vegetated Terrain Conditions

Orhan Eroglu [Member, IEEE], **Mehmet Kurum [Senior Member, IEEE]**, **John Ball [Senior Member, IEEE]**
Department of Electrical and Computer Engineering, Mississippi State University, MS 39759 USA

Abstract

Global navigation satellite system reflectometry (GNSS-R) has the potential to offer a cost-effective solution for global land observations. In this study, we aim to understand GNSS-R sensitivity to changing land geophysical parameters. For this objective, we performed simulations of a ground-based receiver using a recently developed coherent bistatic vegetation scattering model (SCoBi-Veg) to detect GNSS-R signatures under varying soil moisture (SM), vegetation water content (VWC), and surface roughness during a full corn growing season. We modeled different corn growth stages by using *in situ* measurement data. We analyzed the simulated reflectivity and received power values based on the aforementioned variable input parameters. This study demonstrates that specular reflections dominate the diffusely scattered contribution in case of moderate roughness, regardless of the corn field row structure or the polarization. Significant correlations between VWC and cross-polarized reflectivity values are also shown. Furthermore, the study quantifies the effects of SM and surface roughness on GNSS-R deliverables.

Index Terms—

Bistatic scattering; coherent model; global navigation satellite system reflectometry (GNSS-R); signals of opportunity (SoOp); soil moisture (SM); specular reflection; vegetation water content (VWC)

I. Introduction

SOIL moisture (SM) is a key land geophysical parameter on the water, energy, and carbon fluxes through the ground–air boundary of the earth because it is a major component governing the high energy-demanding evapo-transpiration processes. Understanding the SM with high spatial and temporal resolutions at global scales can help improve applications such as crop yield, weather, and natural hazards (e.g. flood, landslide, and drought) forecast [1]–[3].

Global SM sensing is a difficult, complex problem due to challenges arising from sensor technologies, observation geometry, atmospheric losses, and spatial SM variations. Microwave remote sensing, particularly at *L*-band, has been used for this purpose for

Corresponding author: Orhan Eroglu. oe79@msstate.edu.

decades because of its sensitivity to SM and other geophysical parameters [4]. Conventional microwave methods use passive or active mono-static instruments such as radiometers or radars, respectively. For example, NASA's Soil Moisture Active Passive [5], ESA's Soil Moisture Ocean Salinity (SMOS) [6], and Japan's Phased Array *L*-Band Synthetic Aperture Radar [7] are current space missions with *L*-band mono-static radars and/or radiometers that monitor geophysical parameters.

Key limitations of such traditional remote sensing methods are problems with their spatiotemporal sampling, which are often characterized by either coarse resolution with frequent revisit times, or high spatial but low temporal resolution. For instance, the spatial resolutions are 25–50 km for radiometers and tens of meters to few kilometers for mono-static radars, while the temporal revisit times vary from few days for radiometers to few weeks for radars. This hampers the use of such techniques to effectively observe SM for agriculture and hydrometeorology applications that often require both high spatial and high temporal resolutions [8]. The signals of opportunity (SoOp) technique, on the other hand, has recently gained an increasing attention in earth science research community as a promising approach to improve spatio-temporal resolutions for microwave remote sensing of SM. It is based on reception and assessment of the reflected signals from earth's surface in a multi-static scheme, which are already emitted by existing illuminators such as navigation and communication satellites [9]. In particular, global navigation satellite systemreflectometry (GNSS-R) has been widely studied as an application domain of SoOp. The large number of satellites in any GNSS constellation (such as GPS, GLONASS, Galileo, and BeiDou) in the medium earth orbit allows for frequent revisit times [10]. Several small-form factor GNSS-R satellites can be launched in a GNSS-R constellation as well, which also improves the revisit times. Moreover, the spatial resolution for land can fall under even 1 km in theory since the coherent (specular) reflection through the first Fresnel zone is expected to be dominant [11]. Thus, GNSS-R has the potential to provide global coverage with high spatiotemporal resolution by using small size, weight, power, and cost receivers in small satellites.

Several recent studies examined GNSS-R suitability for land remote sensing. Most of them are field experiments with towers or airborne instruments. A reasonable number of these studies measure the interference between the direct and the reflected signals by means of a ground-based, horizontal-looking, geodetic GNSS receiver. Examples of experimental studies that employ this method to retrieve SM, vegetation height, and surface topography over bare or vegetated terrains are reported in [11]–[17]. Some other ground-based polarimetric measurements were also performed [18], [19]. There exist a number of airborne experiments that exploit specially designed GNSS receivers to use polarimetric measurements for SM and biomass sensing [11],[20]–[22].

Several researchers focused on the use of the GNSS-R approach from space such as the qualitative analysis of the UK TechDemoSat-1 (TDS-1) data over land [23]–[25]. The major contribution of this group is to evaluate the feasibility of TDS-1 observations for land applications. Generally, such qualitative works compile comparisons and possible correlations between TDS-1 land returns and other satellite missions that are dedicated to particular retrieval tasks. For example, Camps *et al.* [23] demonstrate TDS-1's sensitivity to

a wide range of SM over terrains with various vegetation covers. They perform a sensitivity analysis by comparing TDS-1 data to the SM data of SMOS and normalized difference vegetation index data of moderate resolution imaging spectro-radiometer missions.

Very few studies utilize scattering models for detailed analysis of factors influencing the received signal in bistatic configuration. Such studies are mainly based on either radiative transfer theory [26]–[30], or analytical wave theory in conjunction with distorted Born approximation [31]–[33]. The former group consists of models that combine the coherent specular reflectivity with the incoherent scattering using the energy conservation principle, while the latter group includes coherent models that provide coherent sum of complex scattered fields. These bistatic models have been applied to diverse terrains such as bare soil, crop fields, and tree canopies under various combinations of linear and circular polarizations and microwave configurations ranging from *P*- to *S*-band. In fact, such a wide applicability is the major strength of the model and simulation studies; they can enable earth science community to explore bistatic configurations and methods.

The main issue for application of GNSS-R to spaceborne instruments stems from the incapability of experimental and comparative studies to quantify the joint impact of distinct parameters, and the insufficient modeling effort that can accurately describe the effect of SM and other parameters. Besides, such a shortcoming often causes some puzzling conclusions through the interpretations of the results. For instance, Camps *et al.* [23] observed diverse SNR and reflectivity trends for bare and sparsely vegetated terrains with very similar surface characteristics. This may be due to the fact that high topographic relief may have led to a dramatic increase in the incoherent scattering, whereas the coherent reflection dominates in other land observations. Furthermore, it may have been caused by spatial SM variations as well. Chew *et al.* [24] found that the direct proportion between the reflectivity and the SM gets satisfied with a sufficiently large dielectric constant for some cases. All in all, such puzzling or qualitative findings indicate the further work needed to quantify the conjunct impacts of different geophysical parameters.

The key contributions of this study is to model a realistic corn crop for accurately representing the vegetation effects, to demonstrate GNSS-R signatures for eliminating the previous puzzling findings, and to help develop generic analytical models for geophysical land parameter retrieval. Therefore, this paper aims to 1) quantitatively compare specular and diffuse contributions by analyzing the co-polarized and cross-polarized received power for varying vegetation and ground conditions, and 2) analyze correlations between the co-polarized and cross-polarized GNSS-R signals and the dynamic parameters (such as SM, vegetation water content (VWC), and surface roughness). In order to achieve these objectives, the study employs our recently developed coherent bistatic vegetation scattering model titled Signals of opportunity Coherent Bistatic scattering model for Vegetated terrains (SCoBi-Veg) [33], and its simulator [34].

The remainder of this paper is organized as follows. Section II describes the SCoBi-Veg model that is employed in the simulations. It then provides the details of the simulation setup and the virtual corn modeling. Section III illustrates the results of the simulations and

presents a comprehensive discussion about significant findings. Section IV concludes the major aspects and the potential future of this study.

II. SCoBi-Veg Model And Simulation Setup

The SCoBi-Veg model and the simulator predicts polarimetric bistatic reflections over vegetated or bare terrains, where the ground is assumed to be flat with a smooth to moderate surface roughness level [33]. It is specialized to the most common SoOp configuration, which consists of a transmitter far-away from the earth surface and a receiver at a low altitude. Fig. 1 depicts such an arrangement over a row-structured crop field. The Fresnel zones that are discriminated by multiples of half-wavelength (unique phase differences) and the receiver footprint are also shown. The east–north–up coordinate system is used as a reference frame to relate the transmitter, receiver, and local coordinates to each other. In the figure, the point S represents the specular reflection point, where the incident and reflected waves make the same angle of θ_s with the surface normal. The azimuth orientation is represented by the angle ϕ_s, which is defined between the ground range and the local north direction. The quantities h_r and h_t represent the receiver and transmitter altitudes, respectively. The range term r_d denotes the line-of-sight distance between the transmitter and the receiver, r_{st} is the distance between the specular reflection point and the transmitter, and r_{sr} stands for the distance between the specular reflection point and the receiver.

SCoBi-Veg applies analytical wave theory in conjunction with the distorted Born approximation to describe vegetation propagation and scattering. The surface roughness under the vegetation is smooth and follows Kirchhoff's approximation with a Gaussian height distribution, so no incoherent scattering from ground is considered. As a typical forward model, SCoBi-Veg demands several input parameters such as transmitter and receiver specifications and orientations, vegetation characteristics, ground soil texture, roughness, and SM. The transmitter and the receiver effects such as polarization crosstalk and mismatch, and orientation are explicitly included through normalized radiation pattern matrices and the polarization basis rotation matrices. The model calculates received specular (coherent), diffuse (incoherent), and direct contributions independently. In addition to the phase information retained for interferometric analysis, the complex field quantities are also converted into the modified Stokes intensity vectors, given by

$$\underline{P}_m^{\mathrm{coh}} = \left\{ \frac{|K|^2}{\left(r_{st} + r_{sr}\right)^2} \right\} \underline{\Gamma}_s \quad (1)$$

$$\underline{P}_m^{\mathrm{inc}} = \left\{ \frac{|K|^2 A_s}{4\pi r_{st}^2 r_{sr}^2} \right\} \underline{\sigma}_e^0 \quad (2)$$

$$\underline{P}_d = \left\{ \frac{|K|^2}{r_d^2} \right\} \underline{D} \quad (3)$$

where

$$|K|^2 = \left(\frac{\lambda_0}{4\pi} \right)^2 G_{0r} \mathrm{EIRP}. \quad (4)$$

From (1) to (3), each underlined term represents a four-by-one modified Stokes vector to describe the wave intensity and polarization. The vectors $\underline{D}$, $\underline{\Gamma}_s$, and $\underline{\sigma}_e^0$ denote direct signal, specular reflectivity, and effective normalized bistatic radar cross section (NBRCS), respectively. The quantity $/K|^2$ is a constant that involves free space wavelength (λ_0), the maximum gain of the receiver antenna (G_{0r}), and the equivalent isotropically radiated power (EIRP) of the transmitter. The quantity A_s is the contributing surface area, where the diffuse scattering originates.

The specular reflectivity $\underline{\Gamma}_s$ involves the wave attenuation as the wave propagates down from the top of the vegetation to the ground, reflection from the surface specularly, and again attenuation from the ground to the top of the vegetation. The surface reflection is assumed to be coherent where smooth-ground Fresnel reflection is used. The reflectivity is essentially attenuated twice by the vegetation. The attenuation and phase change of the coherent wave, propagating in the equivalent medium, is found by calculating the mean field within the medium.

The “effective” NBRCS is acquired through a Monte Carlo scheme that generates a sufficient number of realizations for canonical scatterers within the vegetation canopy. It includes the spreading loss, and the path-dependent phase terms for different diffuse mechanisms in the various multipath directions for all the scattering particles. An average effective NBRCS is obtained by 20 realizations of the vegetation layer through Monte Carlo simulations for the simulations described in the following section. The term “effective” in front of NBRCS comes from the fact that the antenna characteristics as well as the statistical and physical properties of the terrain are blended in NBRCS, since the antenna radiation pattern projected on the surface is not uniformly distributed in phase, amplitude, or polarization for ground-based systems.

Finally, the direct signal $\underline{D}$ represents the signal received through direct line of sight and is included in this section for the sake of completeness even though the direct signal is not used in the analysis here. Expansion of the terms in (1)–(4) and further details can be found in [33].

A. Simulation Setup

This study aims to simulate GNSS-R response to a row-structured crop field under dynamic scene conditions and to observe its sensitivity to several geophysical and system parameters. To generate large synthetic data, snapshots of combinations of a set of these dynamic parameters were simulated for a typical GNSS-R bistatic geometry as illustrated in Fig. 1. The transmitter is a GPS satellite operating with right-hand circular polarization (RHCP) at 1575.42 MHz (L1 C/A-band) with a fixed EIRP of 27 decibels (dB). The receiver is a dual-polarized [RHCP and left-hand circular polarization (LHCP)] antenna system situated at 20 m above ground (a typical tower height). The receiver antenna is modeled as a circularly symmetrical generalized Gaussian pattern with a half-power beamwidth of 30°, side-lobe level of 30 dB, and cross-polarization levels of 15, 25, and 40 dB. The coherent and incoherent processing receiver gain can also be added to the received power in (1)–(3), but it will not change the sensitivity other than introducing an offset to the power values, provided that the thermal noise is not considered. The main beam axis of the receiving antenna is chosen to always face at the specular reflection point, which can be seen in Fig. 1. This is for the purpose of directly analyzing the GNSS-R's angular sensitivity for varying incidence angles by minimizing the antenna pattern effects and polarization mismatch, which might significantly dominate the ground-based observations. As a result, receiver's zenith observation angle is set equal to the transmitter incidence angle (90°—transmitter elevation angle). If the receiver was a nadir-looking antenna, it would require a well-designed omnidirectional pattern to obtain similar results to the present configuration. At the chosen altitude (due to its relatively close proximity to the ground), the receiver antenna footprint limits the contributing area. In other words, diffuse scattering signals coming from the one GNSS chip length (around 300 m) are spatially filtered by the antenna footprint, which falls into approximately the first ten Fresnel zones for the given configuration. Hence, the diffuse scattering power is calculated over the entire footprint (by using ten Fresnel zones); however, effective NBRCS is only considered from the first Fresnel zone to minimize the effect of the system parameters.

The dynamic geophysical and system parameters are the corn growth stages, the zenith observation (θ_s) and azimuth observation (ϕ_s) angles, volumetric SM (VSM), and root mean square height (RMSH) roughness of the surface. Modeling of the corn growth season will be detailed in Section II-B. The zenith observation angle ranges from 10° to 70° by 10° increments. The azimuth angle between the antenna pointing and the plant rows is evaluated for 0°, 30°, 45°, 60°, or 90°. The VSM is varied in the interval of [0.05, 0.40] cm^3/cm^3 by 0.05 cm^3/cm^3 increments. The crop ground is assumed to be flat and to have a typical surface roughness for agriculture, which is modeled uniformly over the ground by three different RMSH values of 0.5, 1.0, and 1.5 cm. For every combination of the dynamic parameter values in conjunction with separate corn growth stages, SCoBi-Veg generates a new database of simulated GNSS-R observations that consist of the direct, specular, and diffuse contributions.

B. Corn Field Modeling

The corn growth stage is the primary dynamic input of the simulating system since it comprises vegetation geometric structure and statistics as well as VWC throughout the

growing season. Physiologically, corn development consists of two major phases, vegetative and reproductive, as shown in Fig. 2. The vegetative phase is the period of rapid growth without cob generation, and it includes VE (emergence), V1 (one leaf) to Vn (n leaves), and VT (Tassel). The reproductive phase is the later period with almost constant plant constituent dimensions, and it involves from R1 (silking) to R6 (maturity). Briefly, the cobs develop from R1 to R4. R5 (dent) is the stage where the kernels are mostly dented at a moisture level around 55%. R6 is the stage with the lowest overall moisture level, where the stalks might still have a moisture content level under their yellowish shell, the leaves are totally dry, and the cobs have a moisture level around 35% [35].

In this study, *in situ* measurement data from the combined radar radiometer 2012 field campaign in Maryland [36] are utilized to account for the temporal evolution of the corn crop. It is a comprehensive study of detailed corn field observations, which include the measurements of plant architecture (dimensions and orientations of stalk, leaves, and cobs), density, VWC, and dielectric constant of vegetation constituents. Canopy measurements except the dielectric constant data were collected roughly once every week during the entire growing season, some instances of which are shown in Fig. 3(a)–(c). In addition, Fig. 3(d) shows canonical shapes that represent vegetation constituents in this study such as thin dielectric discs for leaves [37], [38] and dielectric cylinders for the stalks and cobs [39], [40]. The dielectric constants of the corn stalks, leaves, and cobs were measured at only five different dates during the season (13th July, 1st and 23rd August, 8th and 20th September). To be more precise about the *in situ* vegetation dataset, it includes the height, bottom and top node diameters, and multiple node/internode dielectric constants of the stalk; the length, width, and dielectric constant of the leaf; and the length, diameter, and multi-point (outer, inner, bottom, center) dielectric constants of the cob. The soil is characterized by a soil texture with a sand fraction of 0.60, clay fraction of 0.16, and bulk density of 1.25 g/cm^3. It should be also noted here that the year of the experiment was very dry, which affected the measurements. However, it is not a critical constraint on analyzing the relative sensitivity of the GNSS-R to varying parameters.

The corn growth stages are divided into five different groups to represent the variations in size and moisture content throughout the season by separating the measurement data into five intervals. This is done with respect to VWC amount, constituent dimensions, and cob existence in each measurement period. The two vegetative stage groups are represented by V1–V9 and V10–VT while the three reproductive stage groups are denoted by R1–R4, R5, and R6. The V1–V9 stage represents the rapid emergence of the plant in its infancy period whereas the V10–VT stage accounts for the next rapid growth until the reproductive phase. The R1–R4 phase corresponds to the highest VWC level and largest constituent dimensions (including the cob) within the season while the R5 and R6 periods represent the physiological stages with the same names and their corresponding conditions as described before.

Fig. 4 provides the VWC and dielectric sampling dates, and measured VWC values for stalks, leaves, and cobs and the growth stage separations with different colors. As can be seen from the figure, V1–V9 spans from the emergence to June 26, V10–VT is modeled from the data between June 26 and July 17, R1–R4 covers the middle of the season, R5 is in

the interval that starts with August 15 and ends with September 19, and R6 stands in the senescence period. Measured dielectric dataset is available for all growth stages except V1–V9, whose dielectric constant is assumed to be equal to that of the V10–VT due to its close phenomenology. Fig. 4 also shows that stalk and leaf VWC levels increase as the corn grows until the mid-season (R1–R4), then decrease gradually to the maturity (R6). The cobs emerge in the last week of July 20 and then follow similar growth trend. All in all, R1–R4 has the highest overall VWC whereas V1–V9 and R6 represent the lowest levels. V10–VT and R5 have similar VWC amounts; however, it should be kept in mind that there are cobs in R5 stage that can be an important source of diffuse scattering.

The corn canopy, both individual plant architecture and the entire crop-field structure, is realistically modeled as a detailed virtual three-dimensional row-crop field for the sake of accurately simulating the scattering. Every corn plant is a realistic conjoint body with a stalk that is vertical and fixed on the ground, and corresponding leaves and cobs that are attached to that stalk. Cobs are inserted to the stalk between one and three-fourths of the stalk height, while leaves are inserted above one-fifth of the height through the top of the stalk. To create every individual constituent, *in situ* measurements (dimensions, orientation angles, and dielectric constant) within the growth stage of interest are utilized by fitting distinct probability distributions to those measurements to generate random variables that represent that growth stage. In other words, the orientation and dimensions of the stalk, leaves, and cobs in every individual corn plant are generated by a random process regarding the obtained probability distributions from the field data. The dielectric constants to the constituents are assigned by using the corresponding average dielectric measurement with a five percent standard deviation to accommodate possible variations within each stage. Due to the use of probability distribution functions, every corn plant becomes unique but represents the characteristics of its growth stage. In addition, all of the constituents are involved in the attenuation calculations, whereas leaves are neglected for the diffuse scattering calculations because the leaf thickness is much smaller than the wavelength.

Fig. 5 shows the average measured dimensions and their standard deviations for the stalks, leaves, and cobs for each growth stage. The stalk height, leaf length and width, and cob length exhibit an apparently similar trend to the overall VWC levels, where they have lower values in the emergence and maturity stages and higher values through the mid-season. Hence, V10–VT and R5 generally have medium-scaled values between the season extrema. There exist a few unexpected dimensional behaviors as well. For instance, the stalk diameter slightly decreases during R1–R4 compared to the previous stages. Moreover, the cob diameter gradually increases throughout the entire season. Such behaviors seem abnormal for the physiological development of corn and are interpreted as the experimental biases. However, in general, there is a consistent growth until R1–R4, then there is a shrinkage through the senescence stage.

The vegetation layer consists of rows, as visualized in Fig. 1. The spacing between adjacent rows and corn seeds are 0.75 and 0.20 m, respectively. Moreover, seed positions are generated by means of a quasi-periodic approach, where they may fluctuate in a small circle with a radius of 1.5 cm [41]. Fig. 6 depicts the row structure and the quasi-periodic seed distribution for a small portion of the field. This setting results in a realistic row crop with a

plant density of around 6.7 stalks/m^2. In order to acquire the entire corn field, a sufficiently large square-shaped region that covers all ten Fresnel zones, which is enough for the entire antenna footprint, is first calculated. Then, the seed positions in this region are included in the simulation if they fall into any of the Fresnel zones. Depending on transmitter antenna incidence angles (from 10° to 70°), field size and plant numbers in the field are varied. In addition, the various azimuth angles (0°, 30°, 45°, 60°, and 90°) between the antenna orientation and the plant row are tested to inspect the effect of relative row orientations on GNSS-R response.

It is worth noting here that *in situ* VWC data are not directly used to model the corn vegetation in this study; instead, those are only exploited for the analysis of the simulation results, which is given in Section III. Hence, the dielectric characteristics of the vegetation layer is only represented by the *in situ* dielectric constants whose average real parts are shown in Fig. 7 for each stage. The figure indicates that even though leaf and cob dielectric constants get very small through the senescence, stalk dielectric measurements tend to stay at a remarkably high level throughout the season. In order to explain the effect of moisture content on the measured dielectric constant values, the VWC of stalks, leaves, and cobs are normalized by the volumes of these constituents in each growth stage. The volumetric moisture contents (VWC per volume) are plotted for each constituents and stages in Fig. 8. It is apparent from the figure that the leaves have high volumetric water content in early and mid stages, and then face a dramatic dehydration through the end of the season. The cobs show a rapid raise in moisture content until the R1–R4, then they dry out through the maturity, as also observed from the work presented in [35]. The figure also indicates that the stalks tend to save their effective moisture content even if they lose some amount, since the variations in the dimensions appear to follow a parallel trend with the absolute moisture content. In other words, it can be seen by a comparison between Figs. 5(a) and 8 that expansions and shrinkages in the stalk dimensions make the normalized moisture content have smooth variations through the season. This phenomenon also seems consistent with the observations in the *in situ* field experiments, where mature stalks still have reasonable amount of moisture content despite their outer shells seem shrunk and entirely dry at the time of senescence. Such an observation on the normalized moisture content of the stalks is significant because it accounts for the dielectric constant of these scatterers over time. In other words, relative change of the stalk dimensions and moisture content avoids a drastic reduction in the volumetric moisture content through the growth season, which consequently prevents dielectric permittivity from severe decline. On the other hand, leaf and cob experience severe dehydration through the senescence, which leads to a lowering of normalized moisture content, and it well explains the low cob and leaf dielectric constants during R6.

III. Results and Discussion

In GNSS-R land applications, it has been often assumed that the coherent term is the dominant contributor to the received signal [11]. Kurum *et al.* [33] have recently provided a comprehensive discussion on the relative significance of the altitude dependence on the coherent and incoherent terms for low-altitude platforms. As can be seen in (1) and (2), the specular reflectivity is multiplied by $1/(r_{st} + r_{sr})^2$ whereas the effective NBRCS is multiplied

by $1/\left(4\pi r_{st}^2 r_{sr}^2\right)$. The multiplication in the diffuse term prevents it from having comparable levels against the specular contribution unless the surface is very rough or topographic relief exists. Also, note that the illuminated area of the incoherent return increases with height partially compensating the effect of the ranges, up to the point it is determined by the system range resolution. The vegetation canopy in [33] is modeled as a randomly distributed ensemble of canonical scatterers located above a flat ground. It can be doubted that this approach represents the accurate diffuse contribution over real vegetation covers. The present study incorporates realistic canopy structures, as described in Section II, to investigate the effect of the crop row structure as well as the plant architecture on calculating the diffuse contribution.

Fig. 9 illustrates the specular and diffuse components of the GNSS-R received power over entire footprint (by using ten Fresnel zones) for the growth stage R1–R4 as a function of zenith observation angle (θ_s). The left-most panel shows cross-polarized (RL-RHCP transmit, LHCP receive) received power for 25 dB polarization crosstalk level only (since the effect of crosstalk was minimal for RL-polarization) while the other panels show co-polarized (RR) received power for various polarization crosstalk levels (15, 25, and 40 dB from left to right), as we will also investigate the effect of antenna impurities on the RR-polarization results. Specular reflection from bare soil is also included as a reference. As a side note, these received powers for both polarizations seem to have intuitive levels when compared with the previous experimental observations. Because such studies generally analyze reflectivity and/or NBRCS instead of the received power, the measurement ranges for those parameters can be substituted into 1) and/or 2) in conjunction with the other system parameter values used in these simulations. For instance, Egido *et al.* [18] performed tower experiments (at 25 m) over a sunflower field and the long-term measured cross-polarized reflectivity was in the range [− 20, 5] dB. Such a range for the reflectivity would indicate a range of around [−175,− 160] dB for the cross-polarized coherent received power in this study.

As seen from the left-most panel, it is evident that RL-polarized coherent term is much larger than RL-polarized diffuse contribution. Although the results are limited to 0.15 cm^3/cm^3 of VSM, and 1.0 cm of RMSH in the plots, other combinations of the dynamic simulation parameters (growth stages, VSM, RMSH, and θ_s) that are not depicted here show similar results. It can be concluded that the cross-polarized coherent received power always dominates the incoherent one by far in the case that the surface is flat and smooth (RMSH is under 2.0 cm). This observation supports our implications for the homogeneous vegetation case in [33], and it indicates that the incoherent contribution from vegetation over flat and smooth surfaces can be neglected for studies that take only the cross polarization into account.

The co-polarized received power, on the other hand, shows quite dissimilar behavior compared to the cross-polarized contributions, since ground reflection of a circularly polarized wave gets significantly modified in terms of both polarization and strength. For coherent contribution, the co-polarized power is much lower than the cross-polarized one, but both merge as the angle increases and approaches the Brewster angle. The co-polarized

incoherent term is mostly lower than all the contributions except lower incidence angles, where it gets comparable to co-polarized coherent contribution. It is also apparent from the figure that the incoherent term experiences smoother changes with angles than the coherent term, which has a drastic dependence on the angle. This could be explained by the fact that volume scattering within vegetation combines two polarized components and reduces their relative strength and angular dependence in diffuse scattering. In addition, ideal (no polarization crosstalk and mismatch) antenna results for co-polarized specular term for bare soil and vegetated terrains are also included because, due to the simulated actual antenna, results for bare soil look as if there is a signature at lower angles (the dips in the co-polarized coherent bare soil reflectivity around 40° and 30° for 15 and 25 dB crosstalk, respectively). This behavior happens most likely due to the crosstalk between the receiving antenna ports, which makes a fraction of the signal go into the opposite polarization port. This could be understood by the interference between the leaked cross-polarized and reduced co-polarized contributions as the signals are summed as complex fields. As also evident, the dip and difference between ideal and simulated actual antenna results disappear with 40-dB crosstalk isolation antenna (the right-most result). This indicates that the antenna purity could have a significant effect on co-polarized reflectivity at low-incidence angles and a caution must be exercised if co-polarized contributions are utilized in any retrieval algorithms. Hence, the effects of antenna impurities on co-polarized signals are worth being analyzed separately in a future work. There is one more interesting point on the co-polarized received power that in the ideal antenna case, the coherent vegetation term is larger than the coherent bare soil term at lower angles. The mechanism behind this phenomenon will be explained in detail in the Fig. 12 discussion, which shows this case more apparent with the help of reflectivity analyses.

Although this study indicates that the incoherent contribution is negligible, a remarkable increase in surface roughness or topography, or change in the vegetation cover or bistatic configuration (such as the receiver altitude compared to vegetation height, or the operating frequency of the antennas) can make it comparable to the coherent contribution for both polarizations. For instance, increasing surface roughness can decrease the coherent contribution and increase the incoherent contribution for both polarizations. Another example can be that a different vegetation cover may lead to a reasonable increase in the diffuse scattering while specular contribution stays somewhat constant. This implies that the co-polarized incoherent contribution can deserve to be accounted for depending on the scene characteristics.

Figs. 10 and 11 are aimed at providing a detailed look at the incoherent contribution alone for varying crop row structures. Fig. 10 illustrates the effect of relative orientation of corn crop rows (due to changing antenna azimuth observation angles ϕ_s) on both the co-polarized and cross-polarized effective NBRCS $\underline{\sigma}_e^0$ over the same configuration as in Fig. 9. The effective NBRCS values are plotted for five different azimuth angles in the range 0°, 30°, 45°, 60°, 90°. It is evident that the azimuth orientation of crop rows makes a slight variation (around 0.2 dB) on the effective NBRCS in both polarizations. Hence, this figure indicates that the orientation of the corn field row structure does not have a critical impact on the incoherent component, when the vegetation architecture (plant body structure) remains the

same. This can be attributed to the fact that the diffuse term is driven by the sum of scatterings from individual scatterers within the medium, and large number of scatterers eliminate the azimuth orientation effect. This behavior resembles measurement of the same average physical property sensed by microwave radiometry as it is not affected by the azimuth orientation, too. This can be understood that conservation of energy requires a link between emissivity and reflectivity, demonstrating on basic principles that reflectometry and radiometry measurements are related with each other [42].

Fig. 11 demonstrates a further analysis on the row orientation. Although the main vegetation modeling is based on quasi-periodic seed distribution in our simulations, we also examine a pure periodic row structure with no plant fluctuations in contrast with a random azimuth distribution of plants, while keeping the average vegetation density constant. In the latter case, the row structure of the corn field is completely discarded; however, individual corn plants still keep their architectural features such as constituent dimensions and orientations. In this case, only an azimuth observation angle of 0° is simulated since the effect of the row orientation angle is found to be negligible in the analysis for Fig. 10. Fig. 11 shows that neither periodic, nor random plant distribution can lead to a reasonable difference in the effective NBRCS. Conjunct outcomes of Figs. 10 and 11 imply that diffuse scattering characteristics of the vegetation layer is almost independent from the row structure (orientation and periodicity) while the vegetation architecture remains the same. These conclusions, combined with the observations in Fig. 9, demonstrate dominance of the cross-polarized coherent term; hence, only the coherent term will be analyzed in the rest of the paper.

Fig. 12 represents the reflectivity for both bare soil and vegetated fields, VWC, and leaf area index (LAI) as a function of growth stages. The first panel of the figure shows the cross-polarized reflectivity, LAI, and VWC (the right-vertical axis). The cross-polarized results are given only at 40° since the effect of angular variation and antenna crosstalk were found to be insignificant. On the other hand, the other panels show the co-polarized reflectivity for ideal and simulated actual antenna at various look angles. The purpose of these plots is to describe the relationship between vegetation characteristics and specular reflectivity. In order to determine the effect of the dielectric constant (which varies much for the leaves and cobs, but not much for the stalks, as shown in Fig. 8) on the reflectivity, an additional vegetated reflectivity for cross polarization is provided. To perform this, the dielectric constants of the constituents are set to a fixed value ($40 + i10$), which represents an average value for the entire season. There is no significant difference between the variable and constant permittivity for either cross-polarized or co-polarized reflectivity (the constant dielectric results for co-polarization are not included to keep the plots readable). This can be attributed to the stalk's moisture contents since the stalks are the main contributor to the overall reflectivity, their dielectric constant stays relatively constant, and they retain moisture even in the senescence stage as elaborated in Section II-B.

As seen in the left-most panel of Fig. 12, the cross-polarized reflectivity seems to be significantly related to the VWC/LAI throughout the growing season. The reflectivity increases as the VWC/LAI decreases, and vice versa. For instance, R1–R4, which is the growth period with the highest VWC/LAI level, has the minimum cross-polarized

reflectivity of the season. Similarly, V1–V9 and R6, and V10–VT and R5 exhibit very similar reflectivity trends because they have almost the same VWC/LAI level. This phenomenon can be understood since dielectric permittivity depends on the average water content per volume, but the attenuation is driven by the overall VWC. It is worth repeatedly underlining here that the VWC measurements are not directly involved in the modeling of different growth stages in this study. Instead, the dielectric constant is used to account for separating the dielectric permittivity of the stages. However, the figure shows a strong correlation between the cross-polarized reflectivity and the *in situ* VWC/LAI measurements for each growth stage. These observations imply that at least the cross-polarized reflectivity is mainly determined by overall VWC/LAI level for a configuration of fixed VSM, RMSH, and zenith observation angle. The dynamic range due to growth stages seems to be around 6 dB in this figure. On the other hand, it should be noted that real-world measurements might not be as sensitive as in these simulated results because of several degrading factors (such as measurement errors and noise), despite exhibiting the same trends. For instance, the tower experiments measured at 25 m [18] showed a VWC sensitivity of 0.3 dB/(Kg/m^2) for a sunflower field.

One can further relate VWC levels per growth stages to Figs. 5, 7, and 8 that represent the average constituent dimensions, normalized moisture content by volume, and average dielectric constants for growth stages, respectively. For instance, VWC levels for V1–V9 and R6 are almost the same because of the fact that plants in the R6 carry as much VWC as V1–V9, thanks to their stalk heights and reasonable amount of average moisture content. In addition, stalks rather than leaves or cobs likely dominate the reflectivity as they have the highest VWC level regarding the three figures again. A further interpretation of the findings of Figs. 7 and 12 together can be that the dielectric constant can be kept constant for investigation involving global land observations, where detailed dielectric information is often lacking.

The cross-polarized reflectivity levels for both bare soil (about−10 dB) and vegetation cover (roughly from − 18 to − 12 dB) appear to be realistic when compared with the field data mea sured by Egido *et al.* [19] from an airborne platform over similar scene conditions. Although it is not directly comparable to the in-season changes in this study, the dynamic range due to varying crop types (such as ploughed, sunflower, and barley) in [19] is at similar levels. On the other hand, Katzberg *et al.* [11] observed no reflectivity change between the early and the late stages of the corn development. Possible causes of such an experimental observation can be that 1) early and late stages may resemble one of our growth stage pairs that lead to similar reflectivity levels as mentioned earlier (such as V1–V9 and R6, or V10–VT and R5), and 2) noise might have suppressed the reflectivity changes.

The co-polarized reflectivity does not seem to be inversely correlated with VWC and LAI at the low-incidence angles as seen in the other five panels in Fig. 12, where co-polarized reflectivity is plotted for incidence angles at 30° to 70° from left to right. In these plots, red curves represent the results with the simulated actual antenna (25 dB crosstalk) while the blue curves denote ideal antenna results. At low angles, the discrepancy between ideal and simulated actual antenna is also significant, but as the angle increases, the co-polarization response starts to resemble cross-polarization response and to get correlated with vegetation

characteristics. In addition, the effect of antenna crosstalk on the results gets disappeared with higher incidence angles as both co- and cross-polarization reflectivities get within a comparable range of values. Egido *et al.* [19] showed a quite similar evidence such that the co-polarized reflectivity over a sunflower campaign approaches to the cross-polarized reflectivity as the incidence angle increases. Their co-polarized reflectivity measurements over several bare soil and crop field campaigns also show that the co-polarized reflectivity values in Fig. 12 are at similar levels. Another interesting note is that vegetation reflectivity is higher than bare soil reflectivity at lower angles and as the angle increases it gradually goes below the soil reflectivity. For instance, as can be seen at 40 °, both cross-and co-polarization vegetation reflectivities (the first and third panels, respectively) are sandwiched between bare soil reflectivities. This may seem counter intuitive at the first look. However, this behavior can be explained with the fact that at lower angles, the ground reflection is more in favor of reversing RHCP to LHCP, but LHCP and RHCP merge as the angle increases and vegetation tends to disturb polarization difference of incoming and reflected signals, particularly at lower angles. In other words, vegetation tends to smooth out the polarization difference as this is more apparent at lower incidence angles when the ground reflectivities are very distinct at both polarizations. This means that the vegetation layer does not only make an attenuation effect on the signal power, but it also changes the phase of the signals. For cross-polarized term, there is no surprise that both the attenuation and phase change due to vegetation layer will make the vegetated term lower than the bare soil. However, for co-polarized case, at lower angles, the bare soil term has the lowest reflectivity levels because the ground reflection reverses the RHCP to LHCP. As some vegetation layer is added onto the ground, it will disturb both the RHCP polarization of incoming signals and LHCP polarization of reflected signals and will eventually lead to higher reflectivity values than the bare soil.

Figs. 13 and 14 are dedicated to disclosing the impact of VSM and RMSH on the reflectivity. Fig. 13 demonstrates the cross- and co-polarized reflectivity as a function of VSM in conjunction with the growth stages, when the incidence angle is 30 ° and RMSH is 1.0 cm. While the left-most panel shows RL-polarized reflectivity, the other three panels show the RR-polarized reflectivity for different antenna crosstalk polarization isolation levels (15, 25, and 40 dB from left to right). As seen from Fig. 13, RL-polarized reflectivity increases with increasing VSM levels and seems to reach a saturation when the VSM level is sufficiently large. Therefore, VSM increase of0.5 cm^3/cm^3 can only raise the reflectivity by about 0.1 dB for higher VSM levels, whereas the same change can lead to a jump of around 2 dB for lower levels (total variation of reflectivity from dry to wet SM is about 6 dB, which is significant). A major implication of this can be a reduced GNSS-R sensitivity to high-VSM levels (such as above 0.40 cm^3/cm^3) for cross polarization. On the other hand, one interferometric experiment [16] found distinguishing between lower VSM values (such as 0.05 and 0.10 cm^3/cm^3) to be hard. They also make an important point that the decrease in penetration depth reduces much after heavy rainfall. In such a scenario, the observed values might be lower than the actual VSM levels. This indicates that an inversion model that is capable of finding and handling rapid changes in VSM levels should be developed to overcome such a problem.

RL-polarized reflectivity characteristics of the distinct growth stages are apparent as in Fig. 12. For instance, R5 and V10–VT have almost the same reflectivity for all VSM levels. In general, growth stages do not make an impact on SM sensitivity but instead introduces an offset. Equal sensitivity to VSM variations for different levels of vegetation development (growth stages) is due the fact that the specular vegetation reflectivity involves wave transmissivity, which multiplies the ground reflectivity (i.e., adds transmissivity in the logarithmic scale) as well as the fact that no measurement noise is considered in this study. Therefore, vegetation attenuation only introduces an offset. Under real conditions where noise exists, the estimation of ground reflectivity under dense vegetation will get harder and ground sensitivity will be likely compromised with the other errors such as vegetation attenuation estimation. The effect of VSM on the co-polarized reflectivity generally looks similar to the cross-polarized case for high vegetation, but the effect of antenna impurities such as crosstalk polarization leakage is significant on the light vegetation and bare soil conditions, where there are some abrupt behavior between 0.1 to 0.2 VSM for 15 and 25 dB isolation. Similar to the co-polarized results presented in Fig. 9, abrupt behavior can be attributed that the interference between the leaked cross-polarized and reduced co-polarized contributions as the signals are summed as complex fields. This behavior disappears at 40 dB cross-polarization isolation and the results converge to the ideal antenna results. Egido *et al.* [19] measured the ratio of cross-polarized reflectivity to co-polarized reflectivity as a function of VSM over bare soil fields. Their observation can be related to our cross-polarized (the left-most panel) and co-polarized with 40 dB-XPL (the right-most panel) simulations since they selected the receiving antennas' XPL to exceed 25 dB at boresight to prevent polarization leakage. They observed a linear increase in the polarization ratio, which is also the case for our bare soil simulations. Tower experiments over a sunflower field [18] showed a similar fashion between the cross-polarized and co-polarized reflectivity measurements. Potential future work will attempt to increase the understanding of the abrupt co-polarized behaviors that are attributed to the antenna impurities in this paper.

Fig. 14 additionally introduces the effect of RMSH on the reflectivity for a zenith observation angle of 40° and the R5 stage. For both co-polarization and cross polarization, RMSH has a minimal effect on the reflectivity. For instance, change in RMSH from 0.5 to 1.5 cm produces 1–2 dB variations in the reflectivity as seen from the figure. Moreover, there is no sign of a saturation for the impact of RMSH. However, it should be kept in mind that the SCoBi model processes all these RMSH values as smooth roughness values for a flat surface [33]. Therefore, sufficiently high roughness levels and high topographic relief could dramatically change the results.

IV. Conclusion

In this paper, we presented the quantitative findings for the reflectometric effects of land geophysical parameters such as SM, surface roughness, and VWC by using our recently developed scattering model, SCoBi-Veg. We detected a set of significant GNSS-R signatures over the growing season of a row crop corn field that is simulated by using *in situ* measurement data as follows.

1. We demonstrated the dominance of the coherent contribution in both co-polarized and cross-polarized received powers for a flat and smooth surface case.

2. We examined the impacts of possible row orientation variations and plant distributions on the effective NBRCS in order to check if the diffuse contribution would dominate the specular contribution in any case. Results show that the changes in the row structure without any modification in the plant architectures have minimal consequences on the effective NBRCS. These initial findings indicate that the coherent contribution can be considered alone for land applications if, the ground can be assumed as flat and smooth, and if the vegetation layer height is much lower than the receiver altitude.

3. We analyzed the reflectivity and VWC as a function of growth stages, and we found strong correlation between these two for cross polarization. Furthermore, using a constant dielectric permittivity for each plant constituent through the entire season does not lead to a significant change on the reflectivity. This shows that the changing VWC levels highly dominate the cross-polarized reflectivity; however, changing dielectric constants have a limited effect. This is because the dielectric permittivity is determined by the average volumetric water content, whereas the attenuation is driven by the overall VWC. This can help the researchers assume a reasonably fixed dielectric constant value to model vegetation covers.

4. We presented the quantitative effects of VSM and RMSH variations on the reflectivity. The total variation of reflectivity from dry to wet SM is about 6 dB and VSM sensitivity saturates at higher VSM values, whereas RMSH has a minimal impact on reflectivity for moderately rough surfaces.

   It is demonstrated that the antenna crosstalk leakage could have a significant effect on co-polarized reflectivity at low-incidence angles and a caution must be exercised if co-polarized contributions are utilized in any retrieval algorithms.

The simulated studies via forward models, like those presented in this paper can help develop inversion models for estimating the land geophysical parameters, if they can be expanded for various configurations. As a result, modeling and quantification studies as performed in this study have a potential to clarify experimental observations and possible ambiguities.

Acknowledgment

The authors would like to thank the anonymous reviewers for their valuable comments and suggestions to improve the quality of this paper. They are also grateful to D. R. Boyd for his great effort for proof-reading the manuscript.

This research was funded by NASA Earth and Space Science Fellowship Program under Grant 80NSSC18K1329.

Biographies

Orhan Eroglu (M’17) received the B.S. degree in computer engineering from Bogazii University, Istanbul, Turkey, in 2009, and the M.S. degree in computer engineering from Turkish Air Force Academy, Aeronautics and Space Technology Institute, Istanbul, Turkey, in 2013. He is currently working toward the Ph.D. degree with Mississippi State University, Mississippi State, MS, USA.

He was a Senior Researcher with The Scientific and Technological Research Council of Turkey (TUBITAK), Informatics and Information Security Research Center (BILGEM), between 2009 and 2016. He was the Project Manager of the Air Traffic Controller Tower and Radar Simulator project between 2014 and 2016. His research interests include data analysis and machine learning in remote sensing applications and signal of opportunity.

Mr. Eroglu is a NASA Earth and Space Science Fellow (NESSF’18) with his study entitled Unveiling CYGNSS Land Signatures for High Spatiotemporal Soil Moisture Estimation.

Mehmet Kurum (M’08–SM’14) received the B.S. degree in electrical and electronics engineering from Bogazii University, Istanbul, Turkey, in 2003, and the M.S. and Ph.D. degrees in electrical engineering from George Washington University, Washington, DC, USA, in 2005 and 2009, respectively.

He held a Postdoctoral position with the Hydrological Sciences Laboratory, NASA Goddard Space Flight Center, Greenbelt, MD, USA. In 2016, he was an Assistant Professor with the Department of Electrical and Computer Engineering, Mississippi State University, Mississippi State, MS, USA. His research interests include microwave and millimeter-wave remote sensing, RF sensors and systems, radiation and scattering theory, and signals of opportunity.

Dr. Kurum was a recipient of the Leopold B. Felsen Award for excellence in electromagnetic in 2013 and the International Union of Radio Science (URSI) Young Scientist Award in 2014. He is an Early Career Representative for the International URSI Commission F (Wave Propagation and Remote Sensing).

John Ball (M'03–SM'15) received the B.S. degree in electrical engineering from Mississippi State University (MSU), Mississippi State, MS, USA, in 1991, the M.S. degree in electrical engineering from the Georgia Institute of Technology, Atlanta, GA, USA, in 1993, and the Ph.D. degree in electrical engineering from MSU, in 2007. He also holds a remote sensing certificate from MSU.

He is currently an Assistant Professor in electrical and computer engineering with MSU. He has served ten years in industry, six years in federal government, and six years in academia. He is currently the Director of Radar Laboratory, MSU, and the Co-Director of the Sensor Analysis and Intelligence Laboratory, Center for Advanced Vehicular Systems. His research interests include remote sensing, radar signal processing, general sensor signal and image processing, autonomous vehicle signal processing, machine learning, and deep learning.

Dr. Ball is an Associate Editor for the *Journal of Applied Remote Sensing*.

References

[1]. Entekhabi D et al., "An agenda for land surface hydrology research and a call for the second international hydrological decade," Bull. Amer. Meteorol. Soc, 80, no. 10, pp. 2043–2058, 1999.

[2]. Leese J, Jackson T, Pitman A, and Dirmeyer P, "GEWEX/BAHC international workshop on soil moisture monitoring, analysis, and prediction for hydrometerological and hydroclimatological applications," Bull. Amer. Meteorol. Soc, 82, no. 7, pp. 1423–1430, 2001.

[3]. National Research Council, Earth Science and Applications From Space: National Imperatives for the Next Decade and Beyond. Washington, DC, USA: National Academies Press, 2007.

[4]. Wagner W et al., "Operational readiness of microwave remote sensing of soil moisture for hydrologic applications," Hydrol. Res, 38, no. 1, pp. 1–20, 2007.

[5]. Entekhabi D et al., "The soil moisture active passive (SMAP) mission," Proc. IEEE, 98, no. 5, pp. 704–716, 5 2010.

[6]. Kerr YH et al., "The SMOS mission: New tool for monitoring key elements of the global water cycle," Proc. IEEE, 98, no. 5, pp. 666–687, 5 2010.

[7]. Rosenqvist A, Shimada M, Ito N, and Watanabe M, "ALOS/PALSAR: A pathfinder mission for global-scale monitoring of the environment," IEEE Trans. Geosci. Remote Sens, 45, no. 11, pp. 3307–3316, 11 2007.

[8]. Brocca L, Ciabatta L, Massari C, Camici S, and Tarpanelli A, "Soil moisture for hydrological applications: Open questions and new opportunities," Water, 9, no. 2, p. 140, 2017.

[9]. Zavorotny VU, Gleason S, Cardellach E, and Camps A, "Tutorial on remote sensing using GNSS bistatic radar of opportunity," IEEE Geosci. Remote Sens. Mag, 2, no. 4, pp. 8–45, 12 2014.

[10]. Hofmann-Wellenhof B, Lichtenegger H, and Wasle E, GNSS-Global Navigation Satellite Systems: GPS, GLONASS, Galileo, and more. New York, NY, USA: Springer, 2007.

[11]. Katzberg SJ, Torres O, Grant MS, and Masters D, "Utilizing calibrated GPS reflected signals to estimate soil reflectivity and dielectric constant: Results from SMEX02," Remote Sens. Environ, 100, no. 1, pp. 17–28, 1 2006.

[12]. Rodriguez-Alvarez N et al., "Soil moisture retrieval using GNSS-R techniques: Experimental results over a bare soil field," IEEE Trans. Geosci. Remote Sens, 47, no. 11, pp. 3616–3624, 11 2009.

[13]. Rodriguez-Alvarez N et al., “Land geophysical parameters retrieval using the interference pattern GNSS-R technique,” IEEE Trans. Geosci. Remote Sens, 49, no. 1, pp. 71–84, 1 2011.

[14]. Rodriguez-Alvarez N et al., “Review of crop growth and soil moisture monitoring from a ground-based instrument implementing the interference pattern GNSS-R technique,” Radio Sci, 46, no. 6, pp. 1–11, 12 2011.

[15]. Arroyo AA et al., “Dual-polarization GNSS-R interference pattern technique for soil moisture mapping,” IEEE J. Sel. Topics Appl. Earth Observ. Remote Sens, 7, no. 5, pp. 1533–1544, 5 2014.

[16]. Larson KM, Braun JJ, Small EE, Zavorotny VU, Gutmann ED, and Bilich AL, “GPS multipath and its relation to near-surface soil moisture content,” IEEE J. Sel. Topics Appl. Earth Observ. Remote Sens, 3, no. 1, pp. 91–99, 3 2010.

[17]. Chew CC, Small EE, Larson KM, and Zavorotny VU, “Vegetation sensing using GPS-interferometric reflectometry: Theoretical effects of canopy parameters on signal-to-noise ratio data,” IEEE Trans. Geosci. Remote Sens, 53, no. 5, pp. 2755–2764, 5 2015.

[18]. Egido A et al., “Global navigation satellite systems reflectometry as a remote sensing tool for agriculture,” Remote Sens, 4, no. 8, pp. 2356–2372, 2012.

[19]. Egido A et al., “Airborne GNSS-R polarimetric measurements for soil moisture and above-ground biomass estimation,” IEEE J. Sel. Topics Appl. Earth Observ. Remote Sens, 7, no. 5, pp. 1522–1532, 5 2014.

[20]. Masters D, Zavorotny V, Katzberg S, and Emery W, “GPS signal scattering from land for moisture content determination,” in Proc. IEEE Int. Geosci. Remote Sens. Symp, 2000, 7, pp. 3090–3092.

[21]. Brogioni M et al., “The use of GNSS signals for estimating soil moisture: The LEiMON experiment,” in Proc. IEEE Int. Symp. Geosci. Remote Sens., 2010, pp. 5–7.

[22]. Grant MS, Acton ST, and Katzberg SJ, “Terrain moisture classification using GPS surface-reflected signals,” IEEE Geosci. Lett. Remote Sens, 4, no. 1, pp. 41–45, 1 2007.

[23]. Camps A et al., “Sensitivity of GNSS-R spaceborne observations to soil moisture and vegetation,” IEEE J. Sel. Topics Appl. Earth Observ. Remote Sens, 9, no. 10, pp. 4730–4742, 10 2016.

[24]. Chew C, Shah R, Zuffada C, Hajj G, Masters D, and Mannucci AJ, “Demonstrating soil moisture remote sensing with observations from the UK TechDemoSat-1 satellite mission,” Geophys. Res. Lett, 43, no. 7, pp. 3317–3324, 2016.

[25]. Nghiem SV et al., “Wetland monitoring with global navigation satellite system reflectometry,” Earth Space Sci, 4, no. 1, pp. 16–39, 2017. [PubMed: 28331894]

[26]. Liang P, Pierce LE, and Moghaddam M, “Radiative transfer model for microwave bistatic scattering from forest canopies,” IEEE Trans. Geosci. Remote Sens, 43, no. 11, pp. 2470–2483, 11 2005.

[27]. Ferrazzoli P, Guerriero L, Pierdicca N, and Rahmoune R, “Forest biomass monitoring with GNSS-R: Theoretical simulations,” Adv. Space Res, 47, no. 10, pp. 1823–1832, 2011.

[28]. Guerriero L, Pierdicca N, Pulvirenti L, and Ferrazzoli P, “Use of satellite radar bistatic measurements for crop monitoring: A simulation study on corn fields,” Remote Sens, 5, no. 2, pp. 864–890, 2013.

[29]. Pierdicca N, Guerriero L, Giusto R, Brogioni M, and Egido A, “SAVERS: A simulator of GNSS reflections from bare and vegetated soils,” IEEE Trans. Geosci. Remote Sens, 52, no. 10, pp. 6542–6554, 10 2014.

[30]. Wu X and Jin S, “GNSS-reflectometry: Forest canopies polarization scattering properties and modeling,” Adv. Space Res, 54, no. 5, pp. 863–870, 2014.

[31]. Thirion-Lefevre L, Colin-Koeniguer E, and Dahon C, “Bistatic scattering from forest components. Part I: Coherent polarimetric modelling and analysis of simulated results,” Waves Random Complex Media, 20, no 1, pp. 36–61, 2 2010.

[32]. Kurum M, Deshpande M, Joseph AT, O’Neill PE, Lang RH, and Eroglu O, “Development of a coherent bistatic vegetation model for signal of opportunity applications at VHF/UHF-bands,” in Proc. IEEE Proc. Int. Symp. Geosci. Remote Sens, 2017, pp. 4894–4896.

[33]. Kurum M, Deshpande M, Joseph AT, O'Neill PE, Lang R, and Eroglu O, "SCoBi-Veg: A generalized bistatic scattering model of reflectometry from vegetation for signals of opportunity applications," IEEE Trans. Geosci. Remote Sens, 57, no. 2, pp. 1049–1068, 2 2019.

[34]. Eroglu O, Boyd DR, and Kurum M, "Open-sourcing of a SoOp simulator with bistatic vegetation scattering model," in Proc. IEEE Proc. Int. Symp. Geosci. Remote Sens, 2018, pp. 5879–5882.

[35]. Ciampitti IA, Elmore RW, and Lauer J, "Corn growth and development," Dent, 5, p. 75, 2011.

[36]. O'Neill P et al., "L-band active / passive time series measurements over a growing season using the ComRAD ground-based SMAP simulator," in Proc. IEEE Int. Symp. Geosci. Remote Sens., 2013, pp. 37–40.

[37]. LeVine DM, Meneghini R, Lang RH, and Seker SS, "Scattering from arbitrarily oriented dielectric disks in the physical optics regime,"J. Opt. Soc. Amer, 73, no. 10, pp. 1255–1262, 1983.

[38]. LeVine DM, Schneider A, Lang RH, and Carter HG, "Scattering from thin dielectric disks," IEEE Trans. Antennas Propag, 33, no.12, pp. 1410–1413, 12 1985.

[39]. Seker SS and Schneider A, "Electromagnetic scattering from a dielectric cylinder of finite length," IEEE Trans. Antennas Propag, 36, no. 2 pp. 303–307, 2 1988.

[40]. Karam MA, Fung AK, and Antar YMM, "Electromagnetic wave scattering from some vegetation samples," IEEE Trans. Geosci. Remote Sens, 26, no. 6, pp. 799–808, 11 1988.

[41]. Utku C and Lang RH, "Coherence effects in L-Band active and passive remote sensing of quasi-periodic corn canopies," in Proc. 30th URSI Gen. Assembly Sci. Symp, 2011, pp. 1–4.

[42]. Arroyo AA, Camps A, Monerris A, Rudiger C, P Walker J,Onrubia R, "On the correlation between GNSS-R reflectivity and L-band microwave radiometry," IEEE J. Sel. Topics Appl. Earth Observ. Remote Sens, 9, no. 12, pp. 5862–5879, 12 2016.

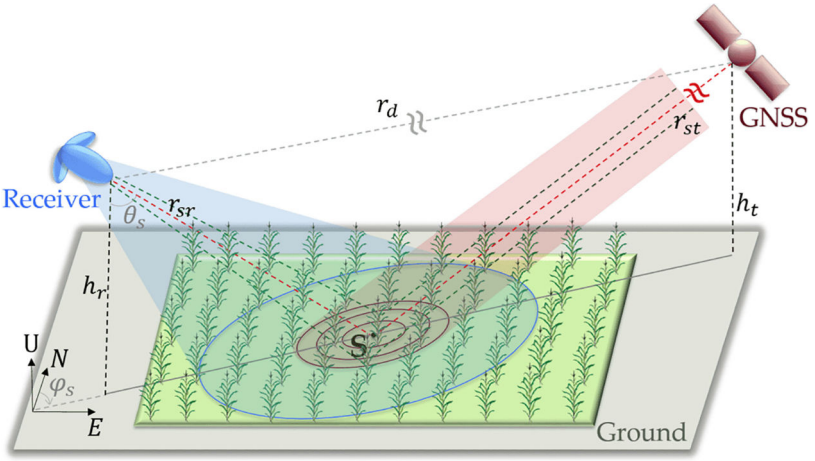

Fig. 1.

Bistatic configuration of the simulations. Transmitter is a GNSS satellite. Receiver is a ground-based, dual-polarized antenna always pointing toward the specular reflection point. Vegetation cover is a row-structured corn field.

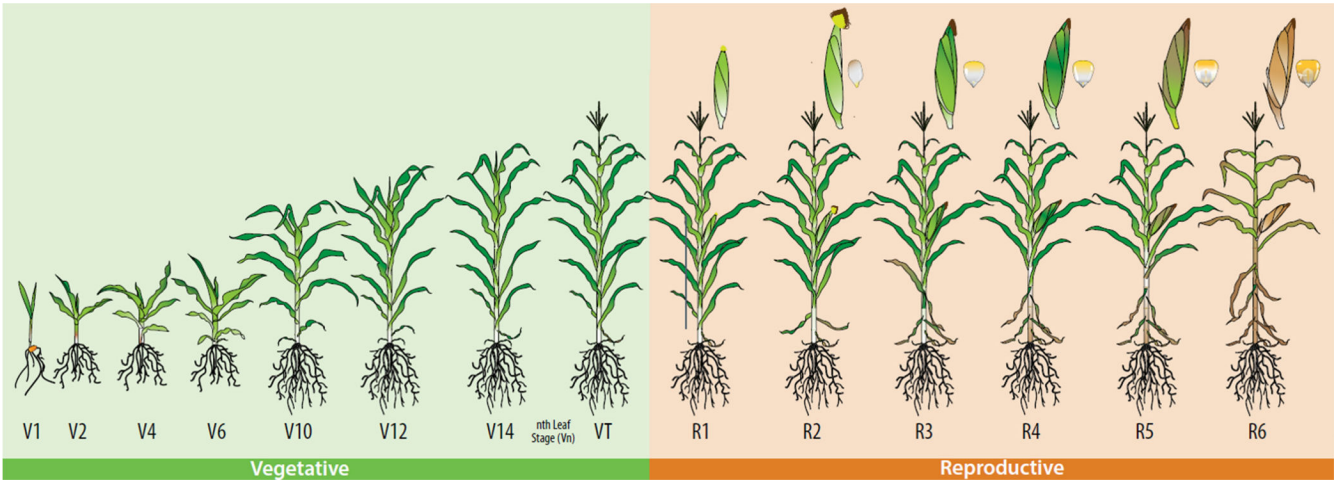

Fig. 2.

Corn growth stages for vegetative and reproductive phases [35]. The vegetative stages are named by the number of leaves, whereas the reproductive stages are named regarding the cob development.

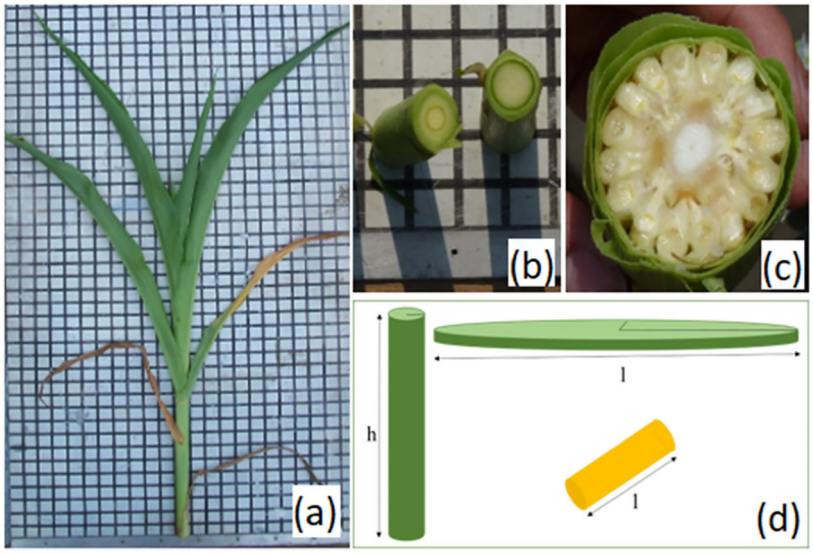

Fig. 3.

In situ measurements and virtual constituent representations. (a) Corn dimension and orientation. (b) Stalk. (c) Cob. (d) Cylinder and elliptic disk to represent stalk and cob, and leaf, respectively.

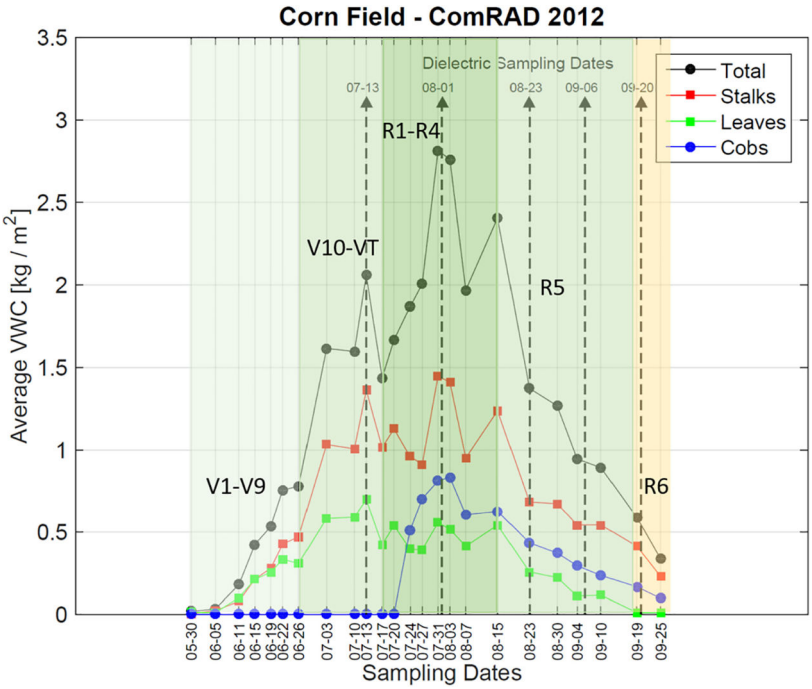

Fig. 4.

VWC measurement dates and values, dielectric measurement dates, and growth stage separation.

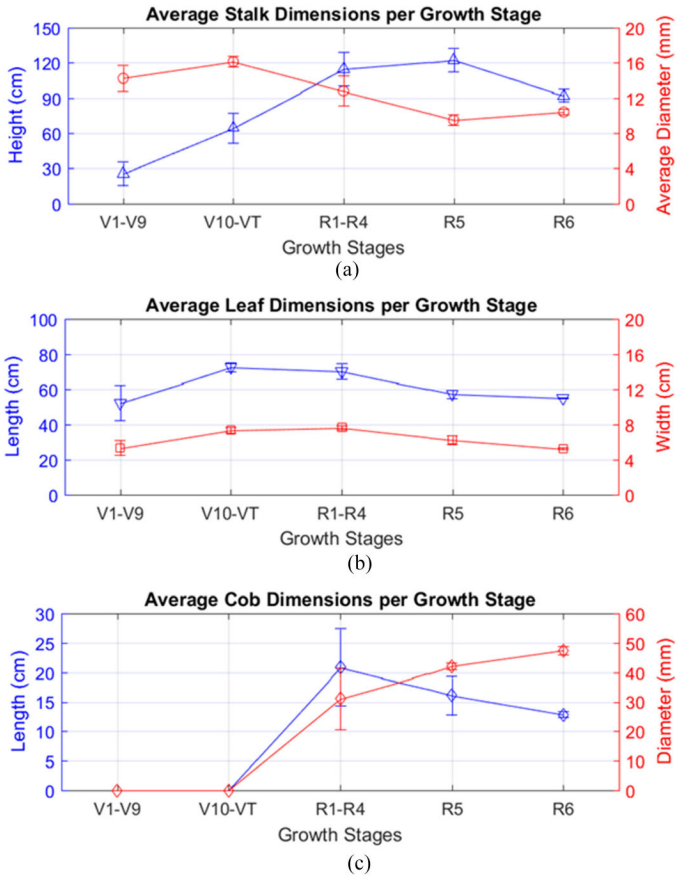

Fig. 5.

Average dimensions for varying growth stages. Error bars indicate the standard deviations. (a) Stalks. (b) Leaves. (c) Cobs.

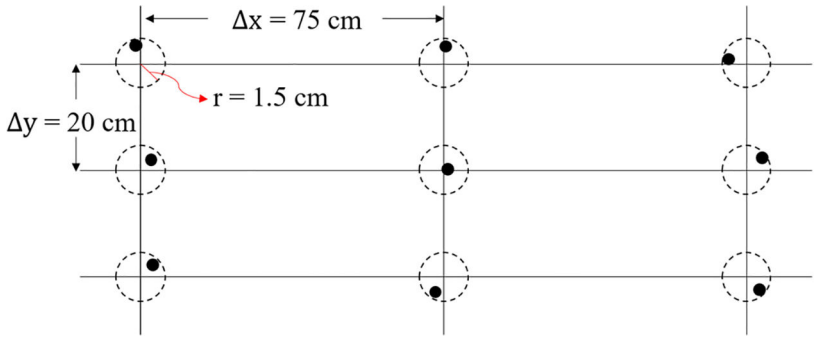

Fig. 6.

Quasi-periodic seed distribution within the row structure. Δ*x*: spacing between rows, Δ*y*: spacing between adjacent seeds in a row, *r*: maximum radius of fluctuation circle.

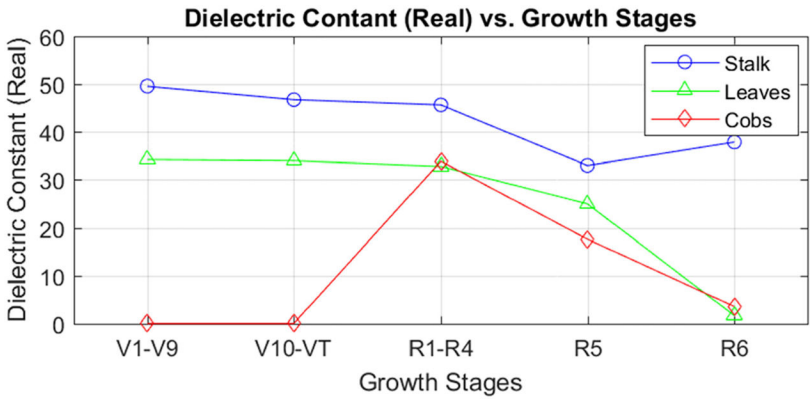

Fig.7.

Average dielectric constant (real part) of the corn plant constituents.

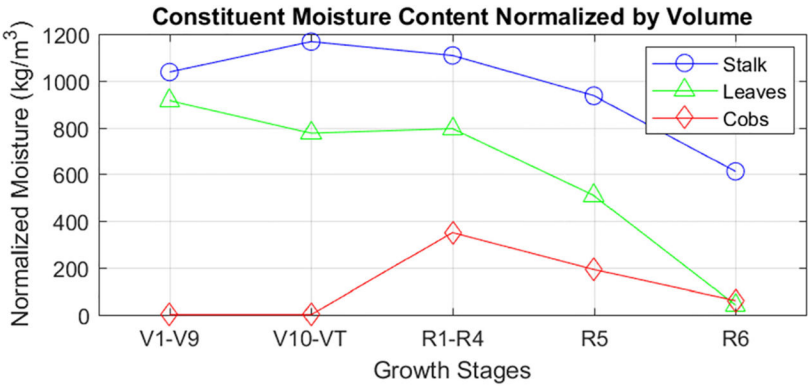

Fig. 8.

Normalized moisture content of the corn plant constituents by their volume per growth stages.

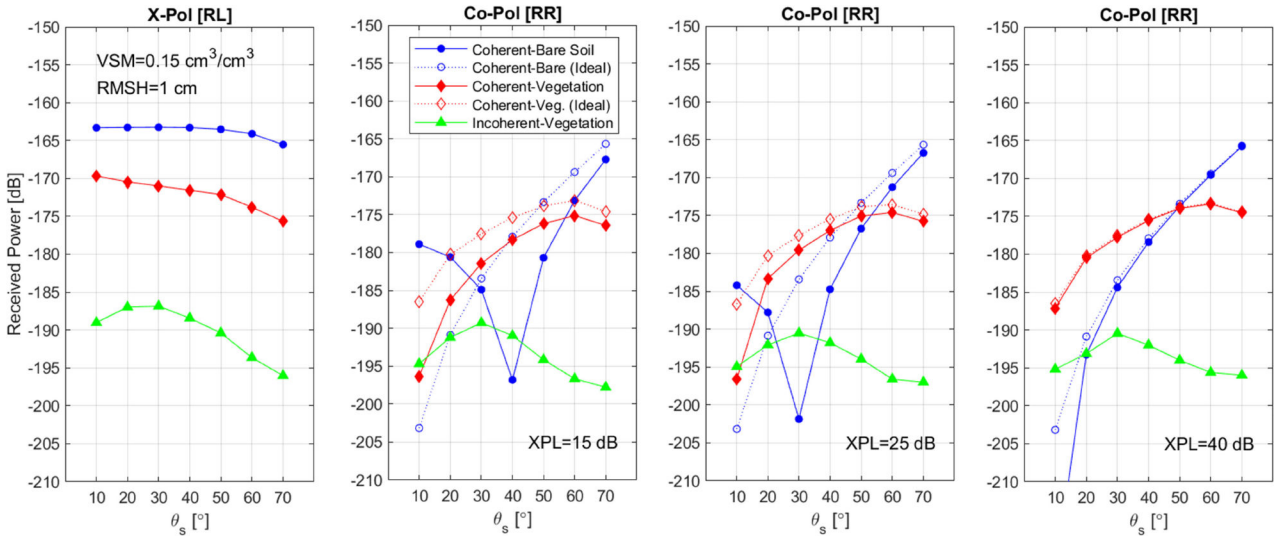

Fig. 9.

Received power coherent and incoherent contributions as a function of zenith observation angle (equal to the transmitter's incidence angle so that incident wave impinging from the specular direction is considered) for the growth stage R1–R4. EIRP = 27 dB. Receiver gain = 0 dB. [The received power will be modified with actual system EIRP, receiver gain, and processing gains (coherent/incoherent integrations).] (RR: RHCP–RHCP, RL: RHCP–LHCP).

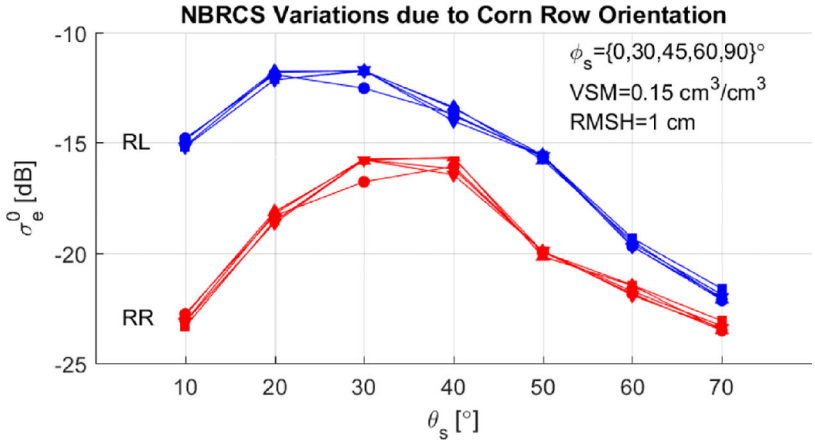

Fig. 10.

Effect of the crop row orientation angles on the effective NBRCS (over the first Fresnel zone) for quasi-periodic seed distribution in the growth stage R1–R4. Each plot in both RR (red) and RL (blue) polarization corresponds to five azimuth angles between antenna observation and the crop rows.

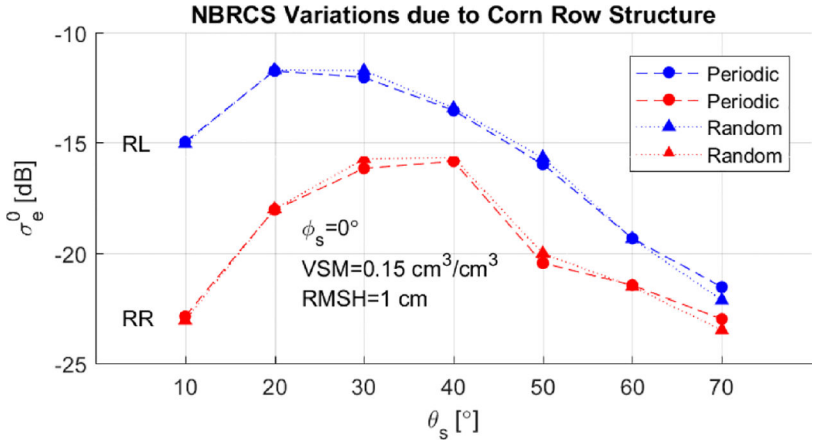

Fig. 11.

Effect of periodic crop row and random seed distribution on the effective NBRCS (over the first Fresnel zone) for both RR and RL polarizations in the growth stage R1–R4.

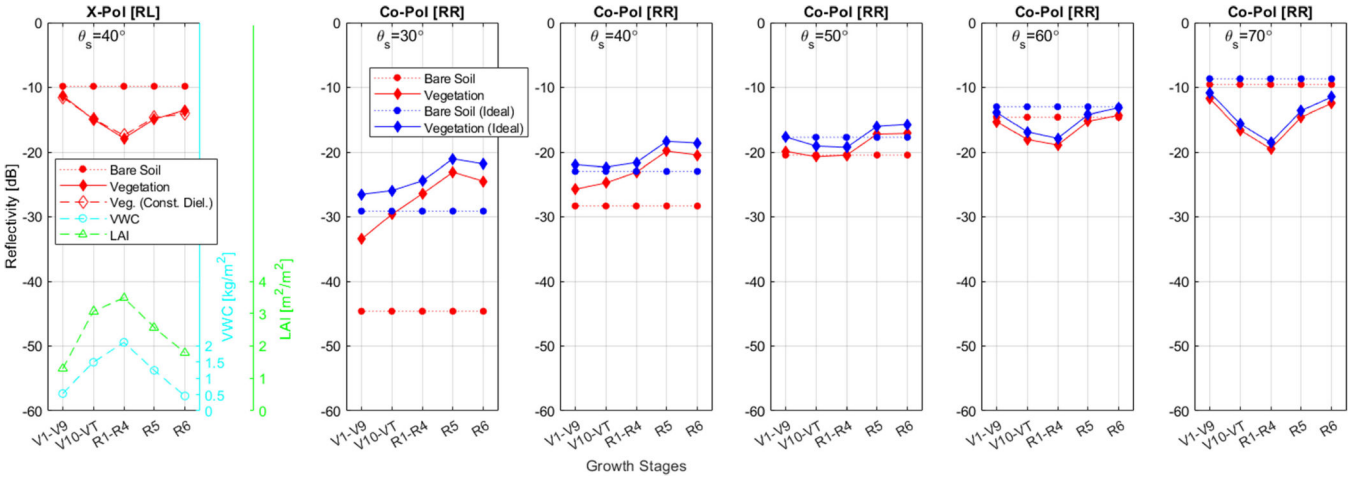

Fig. 12.

Reflectivity, VWC, and LAI as a function of growth stages (VSM = 0.1 cm^3/cm^3, RMSH = 1.5 cm). X-pol reflectivity is given only for simulated actual antenna at $\theta_s = 40°$ since there is no significant difference due to angle variations and antenna impurities for X-pol. Co-pol reflectivity is given for ideal and simulated actual antenna for $\theta_s = 30° : 10° : 70°$ since angle variations and antenna impurities matter for Co-pol. Bare soil reflectivity for both X-pol and Co-pol are given for reference. X-pol reflectivity values for a constant dielectric permittivity $(40 + i10)$ for the entire season are also shown.

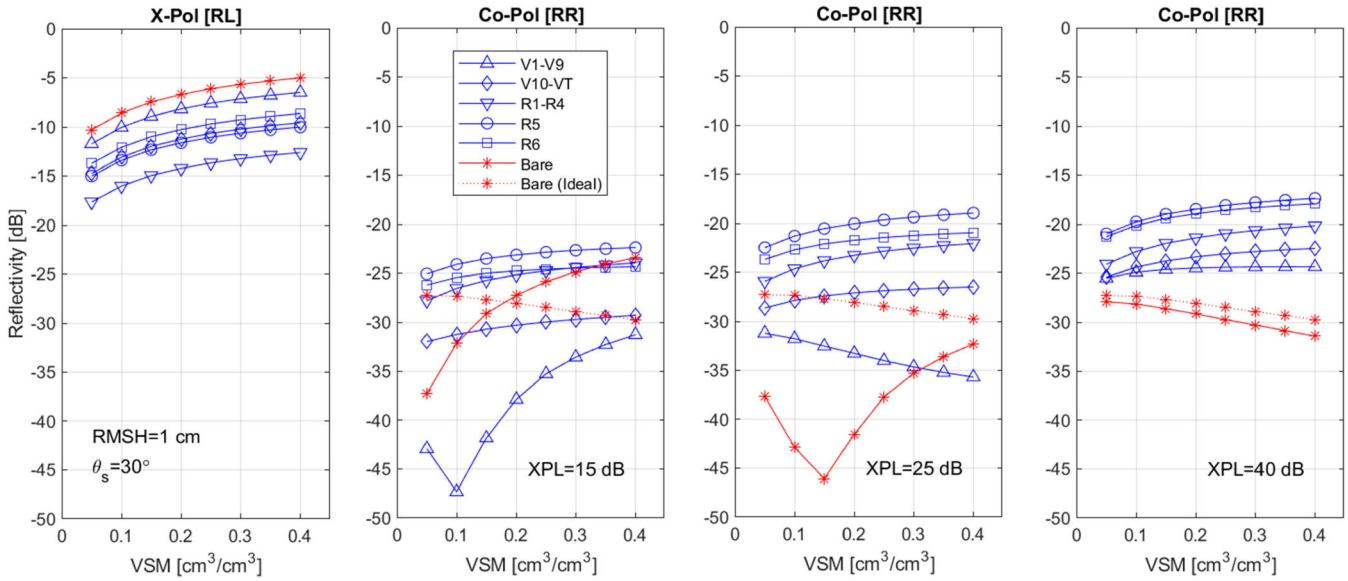

Fig. 13.

Reflectivity as a function of VSM and growth stages. Bare soil reflectivity for both the ideal and simulated actual antenna cases given for reference.

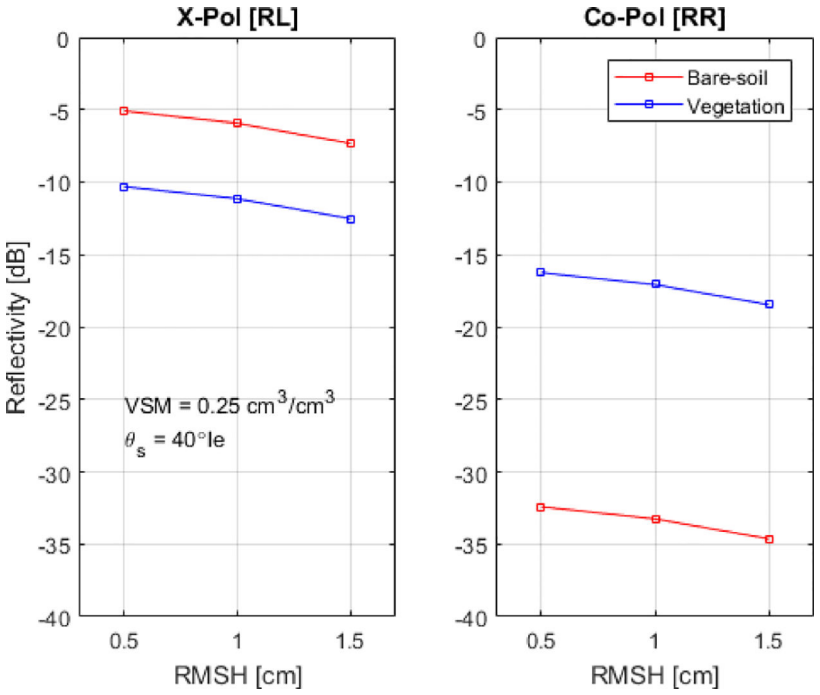

Fig. 14.
Reflectivity as a function of VSM and RMSH variations for the growth stage R5.